Distributed Algorithms for Joint Channel Access and Rate Control in Ultrasonic Intra-Body Networks

Zhangyu Guan, *Member, IEEE*, G. Enrico Santagati, and Tommaso Melodia, *Member, IEEE*

***Abstract*—Most research in body area networks to date has focused on traditional RF wireless communications, typically *along the body surface*. However, the core challenge of enabling networked *intra-body* communications through body tissues is substantially unaddressed. RF waves are in fact known to suffer from high absorption and to potentially lead to overheating of human tissues. In this paper, we consider the problem of designing optimal network control algorithms for distributed networked systems of implantable medical devices wirelessly interconnected by means of *ultrasonic waves*, which are known to propagate better than radio-frequency electromagnetic waves in aqueous media such as human tissues. Specifically, we propose lightweight, asynchronous, and distributed algorithms for joint rate control and stochastic channel access designed to maximize the throughput of ultrasonic intra-body area networks under energy constraints. We first develop (and validate through testbed experiments) a statistical model of the ultrasonic channel and of the spatial and temporal variability of ultrasonic interference. Compared to in-air radio frequency (RF), human tissues are characterized by a much lower propagation speed, which further causes unaligned interference at the receiver. It is therefore inefficient to perform adaptation based on instantaneous channel state information (CSI). Based on this model, we formulate the problem of maximizing the network throughput by jointly controlling the transmission rate and the channel access probability over a finite time horizon based only on a statistical characterization of interference. We then propose a fully distributed solution algorithm, and through both simulation and testbed results, we show that the algorithm achieves considerable throughput gains compared with traditional algorithms.**

***Index Terms*—Distributed algorithms, intra-body area networks, stochastic channel access, ultrasonic communications.**

I. Introduction

WIRELESS intra-body networks have received considerable attention in the last few years [2], [3], driven by the fascinating promise of a future where carefully-engineered miniaturized biomedical devices implanted, ingested or worn by humans can be wirelessly internetworked to provide personalized health care by collecting diagnostic information (e.g., measuring the level of glucose in the blood of diabetic patients) and by fine-tuning medical treatments (e.g., adaptively regulate the dose of insulin administered) over extended periods of time [4], [5]. Networked systems composed of implanted sensors and actuators could enable revolutionary applications at the intersection between biomedical science, networking, and control, e.g., measuring the level of glucose in the blood of diabetic patients, and reactively controlling actuators implanted under the skin to adaptively regulate the dose of insulin administered, or using pill-sized cameras to monitor the digestive tract. Yet, while body area networks have received considerable attention in the last few years [2], [3], most research to date has focused on communications *along the body surface* among devices that use traditional electromagnetic radio-frequency (RF) carrier waves, leaving the root challenge of enabling networked *intra-body* miniaturized (at the micro or nano scale) sensors and actuators that communicate through body tissues substantially unaddressed.

Challenges and New Approaches: Commercial wireless medical implants [6], [7] that communicate through RF point-to-point links have recently become available, along with RF-based transceiver chips for medical implants [8]. However, these technologies tend to merely "scale down" traditional wireless technologies (e.g., Bluetooth, Zigbee) to the intra-body environment, with little or no attention to the peculiar characteristics and safety requirements of the human body. The human body is however composed (up to 65%) of water, a medium through which RF waves do not propagate well. In addition, the medical community is still divided on the risks caused by exposure of human tissues to RF radiation—the World Health Organization classifies RF waves as "possibly carcinogenic to humans". Not less importantly, RF-based technologies are prone to malicious jamming attacks or to environmental interference from pervasively deployed existing RF communication systems that can undermine the reliability and security of the intra-body network, and ultimately the safety of the patient.

For these reasons, in [4], [9], [10] we proposed a different approach and explored *the use of ultrasonic waves to wirelessly internetwork in-body devices, i.e., ultrasonic intra-body area networks.* Acoustic waves, typically generated through piezoelectric materials, are known to propagate better than RF in dielectric media composed primarily of water. Since World War II, piezoelectrically generated acoustic waves have found application, among others, in underwater communications (typically at frequencies between 0 and 100 kHz), in indoor localization [11], and, massively, in ultrasonic medical imaging [12]. While communication at low frequencies requires sizable transducers, innovations in piezoelectric materials and fabrication methods, primarily driven by the need for resolution in medical imaging, have made miniaturized transducers at the micro [13], [14] and

Manuscript received January 23, 2015; revised August 28, 2015 and November 23, 2015; accepted November 24, 2015; approved by IEEE/ACM TRANSACTIONS ON NETWORKING Editor Y. Yi. This material is based upon work supported in part by the National Science Foundation under Grant CAREER CNS-1253309. A preliminary shorter version of this paper appeared in the Proceedings of the IEEE Conference on Computer Communications, Hong Kong, April 2015.

The authors are with the Department of Electrical and Computer Engineering, Northeastern University, Boston, MA 02115 USA (e-mail: zguan@ece.neu.edu; santagati@ece.neu.edu; melodia@ece.neu.edu).

Color versions of one or more of the figures in this paper are available online at http://ieeexplore.ieee.org.

Digital Object Identifier 10.1109/TNET.2015.2510294

even nano scales [15] a reality; with examples of devices that have even reached clinical stages [16].

Envisioned New Applications: Ultrasonic wave heat dissipation in tissues is low compared to RF waves [17]. The medical experience of the last decades has demonstrated that ultrasounds are fundamentally safe, as long as acoustic power dissipation in tissues is limited to predefined safety levels [4], [5]. Therefore, ultrasonic intra-body area networks can improve existing biomedical applications as well as enable a rich set of new applications, which can be as diverse as automated drug administration, pervasive surveillance using pill-size ingestible cameras, bio-hybrid implants, intraocular pressure monitoring, malicious agent monitoring, heart monitoring, and minimally-invasive microsurgery [4].

While in some applications, e.g., in under-skin and static scenarios, implanted sensors can be easily pre-deployed, possibly wired, and scheduled in a centralized fashion, in many envisioned applications this is however undesirable. For example, in *automated drug administration*, targeted drug delivery in a spatial-, temporal- and dosage-controlled fashion based on distributed measures of biological parameters is already a reality [16]. In these scenarios, it is infeasible to wire deeply-implanted devices, and centralized scheduling of interfering wireless links serving different areas of the body may be complex and involve long-range, high-power transmissions that are undesirable due to potential excessive radiation. Another example is *pervasive surveillance*, where malicious agents are monitored through distributed networks of ingestible sensors [18]—in this case centralized control is by no means easy to implement without global network topology information; moreover it may not be easy to maintain global synchronization, which makes distributed control an appealing approach as in traditional mobile ad hoc networks.

Main Contributions: Based on these premises, in this paper we design *lightweight* (i.e., based on local decisions taken through polynomial-time algorithms and with minimal message exchange), *asynchronous* (updates at different nodes are unsynchronized, i.e., as in [19, p. 425]), and *distributed* (i.e., without centralized control) resource allocation algorithms. We claim the following main contributions.

- We develop for the first time (and validate through testbed experiments[1]) new statistical models of ultrasonic interference. The models capture the unique spatial and temporal variability of unaligned ultrasonic interference through a new approach (that we refer to as *M-sampling method*) in which interference is characterized through a vector of measurements taken at multiple instants of time at each receiver during a given interval (i.e., time slot) to capture its statistical behavior. The effects of temporal uncertainty (i.e., the random transmission of different nodes on time-varying ultrasonic channels) on the interference level at each measurement point is modeled using generalized Nakagami probability distribution functions.
- Based on this modeling framework, we formulate an optimization problem where the objective is to maximize the throughput achievable by mutually interfering nodes by jointly controling cross-layer networking functionalities of devices in an ultrasonic network (e.g., channel access, spectrum management, queuing and rate control) while keeping the radiated power within safety limits. A core feature of the proposed algorithm is that decisions at each node are taken based only on the *second-order moment* of ultrasonic interference (and *not* on its instantaneous level). The actual level of interference cannot in fact be known at the transmitter without significant delay and overhead, while its variance varies slowly in time.
- Then, we design and validate through simulations and testbed experiments new probabilistic throughput-maximizing distributed cross-layer control strategies based on these newly developed stochastic models of ultrasonic interference. We show that the proposed joint optimization leads to up to nine times higher throughput with respect to optimizing the transmission profile or rate control individually.

The rest of the paper is organized as follows. In Section II, we review the related work. In Section III, we describe the propagation characteristics of ultrasonic signals in human tissues, and based on our experimental measurement results, we propose statistical models of ultrasonic small-scale fading and interference, respectively. In Section IV, we formulate the optimization problem and then propose a distributed solution algorithm in Section V. In Section VI, we present the globally optimal solution algorithm. Performance of the distributed algorithm is then evaluated through both simulation and testbed results in Section VII, and finally conclusions are drawn in Section VIII.

II. Related Work

In [4], [20], we showed that intra-body ultrasound propagation is severely affected by multipath caused by inhomogeneity of the body in terms of density, sound speed, and the pervasive presence of small organs and particles. Based on these observations, in [9], we proposed Ultrasonic WideBand (UsWB), a new ultrasonic multipath-resilient physical and medium access control (MAC) layer integrated protocol. UsWB is based on the idea of transmitting short carrierless ultrasonic pulses following a pseudo-random adaptive time-hopping pattern, with a superimposed adaptive spreading code. Impulsive transmission and spread-spectrum encoding combat the effects of multipath and scattering and introduce waveform diversity among interfering nodes so that multiple users can coexist with limited interference on the same channel. In [10], we experimentally demonstrate the feasibility of ultrasonic communications in human tissues through an FPGA-based prototype implementation of the UsWB physical and medium access control protocols. We showed that our prototype can flexibly trade data rate performance for power consumption, and achieve, for bit error rates (BER) no higher than 10^{-6}, either (i) high-data rate transmissions up to 700 kbit/s at a transmit power of -14 dBm ($\approx 40\ \mu$W), or (ii) low-data rate and lower-power transmissions down to -21 dBm ($\approx 8\ \mu$W) at 70 kbit/s (in addition to numerous intermediate configurations). Moreover, we show how the UsWB MAC protocol allows multiple concurrent users to coexist and dynamically adapt

[1]Since conducting experiments in real live tissues is complex, in this work the validation is based on a Kidney phantom testbed (see details in Section III), which provides a good approximation of the ultrasonic propagation characteristics of real tissues. In-vivo experiments in real body tissues will be conducted before applying the algorithms discussed in this article in clinical settings.

their transmission rate to channel and interference conditions to maximize throughput while satisfying predefined reliability constraints, e.g., maximum packet drop rate.

There are also some important lessons to be learnt in dealing with acoustic interference from recent research in underwater networks; even though there, the focus is mostly on long-distance, low data rate communications. Significant recent efforts have attempted to address some of the challenges of interference modeling at the MAC layer [21]–[24]. For example, it was shown in [21] that for slotted transmission the packet collision probability can be reduced by adding a guard band to each time slot to limit the effect of the spatial uncertainty of interference. In [22], [25], different MAC schemes based on handshaking were proposed to avoid interference, while the resulting hidden terminal problems were studied in [23]. However, i) these solutions mainly rely on signaling exchanges that still suffer from the low-speed of sound, and might result in under-utilization of the channel and therefore in low throughput; moreover, ii) they look at the problem from a MAC perspective, exclusively. While the above MAC protocols mostly attempt to mitigate the negative effect of spatial uncertainty of interference, Chitre, *et al.* pointed out in [24] that the large hence distance-dependent propagation delay could be exploited through interference alignment (IA) in the time domain to achieve a throughput much higher than that without spatial uncertainty. However, the IA scheme in [24] largely relies on exact knowledge of global location information of all nodes and on centralized control, which is not easy to implement in practice due to high communication overhead required to collect exact location information and to broadcast schedules. Furthermore, iii) no previous work has modeled the temporal uncertainty of interference, i.e., its time-varying nature, and its cumulative effect, and iv) previous work is largely based on the protocol interference model, i.e., a packet is lost whenever two transmissions overlap at a receiver, which is not the case with advanced transmission schemes. Ultimately, v) *existing models fail to capture the statistical behavior of time-varying and spatially uncertain ultrasonic channels*, and moreover, previous work has not considered the asynchronous transmission behavior of each node and are unsuitable to applications with random packet arrivals.

Finally, there is a large body of work on distributed medium access control and cross-layer optimization algorithms for wireless networks (see, among many others [26]–[31]). For example, Huang and Lin proposed a Virtual-Multi-Channel CSMA algorithm [30] while Kwak, Lee and Eun proposed a delayed CSMA based on high-order Markov chains [31], to avoid the starvation problem in traditional CSMA. However, algorithms proposed for RF wireless communications (i) do not consider the spatially and temporally uncertain ultrasonic environment; plus, (ii) most of them typically require coordination and instantaneous and synchronized control message exchanges that are not desirable in resource-constrained environments affected by long propagation delays.

III. Channel and Interference Modeling

Ultrasonic waves originate from the propagation of mechanical vibrations of particles in an elastic medium at frequencies above the upper limit for human hearing, i.e., 20 kHz. Acoustic propagation through a medium is governed by the acoustic wave equation (Helmhotz equation), which describes pressure variation over the three dimensions, $\nabla^2 P - \frac{1}{c^2}\frac{\partial^2 P}{\partial t^2} = 0$, where $P(x, y, z, t)$ represents the acoustic pressure scalar field in space and time, and c is the propagation speed in the medium with a typical value of 1500 m/s in blood and other soft tissues [4] (i.e., five orders of magnitude slower than RF propagation in air).

TABLE I
Frequency Limits for A = 100 dB

Communication Range	Distance	Frequency Limit
Short Range	μm - mm	> 1 GHz
Medium Range	mm - cm	$\simeq 100$ MHz
Long Range	>cm	$\simeq 10$ MHz

In [4] it was shown that attenuation can be significant and it increases (exponentially) with the distance between transmitter and receiver. For example, Table I shows the maximum "allowed" carrier frequency for a 100 dB maximum tolerable attenuation [4], [5]. Note that even with transmission distances of no more than a few tens of centimeters, due to the low speed of ultrasonic signals, the propagation delay can be rather large compared with the channel access period, leading to non-aligned interference and thus making time-division MAC protocols not efficient. Based on the experimental observations from our testbed measurements, next we propose a theoretically tractable interference model for ultrasonic propagation in human tissues. To this end, we first characterize the small-scale fading of the ultrasonic channel—for which unfortunately there is no literature available to date.

Channel Model: We conducted a series of experiments to measure the small-scale fading on the channel with the ultrasonic software defined testbed that we developed. The testbed consists of ultrasonic software defined nodes (uSDNs) communicating through physical medical phantoms (i.e., tissue-mimicking materials with acoustically accurate representations of anatomy) that emulate with high fidelity propagation through biological tissues. The uSDNs are implemented using the Universal Software Radio Peripheral (USRP) N210 software-defined radios interfaced with low-frequency (LFRX and LFTX) daughterboards [32] and ultrasonic transducers operating around 5 MHz with a -6 dB bandwidth of about 4 MHz [33]. Phantoms are interposed between transmitters and receivers to emulate propagation through tissues. In Fig. 1(a) we show a sample experimental setup with a phantom mimicking propagation through a human kidney [34]. We measured the faded envelope of ultrasonic signals,[2] and the experimental result is least-square fitted with a Nakagami and a generalized Nakagami distribution. We found that the

[2]Real intra-body ultrasonic propagation environments are time varying because of the constant movements of human organs. In our experiments, we moved the transducers in Fig. 1(a) to a different location in each instant of channel measurement to introduce variability in the propagation environments. A three-dimensional movement model has been considered to mimic the motion of a real human Kidney [35]. In each measurement, the transducers are displaced following three directions, i.e., superior-inferior, anteri-or-posterior and medial-lateral, and the maximum displacement from the reference point is set to 10 mm, 5 mm and 3 mm in the three directions, respectively.

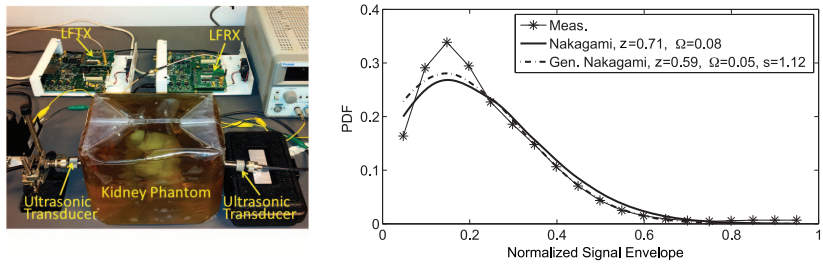

(a) (b)

Fig. 1. (a) Ultrasonic experimental testbed; (b) Measurement and fitting results for the envelope fading of ultrasonic signals.

generalized Nakagami distribution fits the measurement results in general well, as shown in Fig. 1(b), particularly at high signal envelope values.[3] Results indicate that the ultrasonic signals are attenuated by both randomly-located and structured scatterers when propagating through the kidney, corresponding to a Nakagami parameter between 0.5 and 1 (0.59 with generalization parameter $s = 1.12$ according to our measurements in the considered setting). To the best of our knowledge, these are the first measurements reported for ultrasonic communications in tissues.

Motivated by these experimental observations, we model the statistical characteristics of the channel fading coefficient ρ_t for any time slot t using a generalized Nakagami distribution function $\xi(x)$,

$$\xi(x) = \mathrm{P}[\rho_t = x] = \frac{2sz^z x^{2sz-1}}{\Gamma(z)\Omega^z} e^{-\frac{z}{\Omega}x^{2s}}, \qquad (1)$$

where z, Ω and s are the shaping, spreading, and generalization parameters of the generalized Nakagami distribution function that can be measured off-line or estimated online, and $\Gamma(z) \triangleq \int_0^\infty x^{z-1}e^{-x}dx$ is the gamma function.

Then, the channel gain of the ultrasonic link in tissues from transmitter m to receiver n on sub-channel $f \in \mathcal{F}$ at time slot t, denoted by h_{nm}^{tf}, can be represented as[4]

$$h_{nm}^{tf} = H_{nm}^{f} \cdot (\rho_t)^2, \qquad (2)$$

where H_{nm}^{f} represents the transmission attenuation that an ultrasonic signal transmitted on sub-channel $f \in \mathcal{F}$ experiences over a transmission distance d_{nm} [4]. Denote f_c as the central frequency of sub-channel f. Then, H_{nm}^{f} can be represented as $H_{nm}^{f} = e^{-\beta(f_c)\cdot d_{nm}}$, where $\beta(f_c)$ (in $[\mathrm{np} \cdot \mathrm{cm}^{-1}]$) represents the amplitude attenuation coefficient that captures all the effects associated to energy dissipation from the ultrasonic beam. The parameter $\beta(f_c)$ can be further represented as $\beta = a \cdot (f_c)^b$, where a (in $[\mathrm{np\ m}^{-1}\ \mathrm{MHz}^{-\mathrm{b}}]$) and b are attenuation parameters characterizing the tissue that can be measured off-line. In the rest of the paper, we simplify h_{nm}^{tf}, H_{nm}^{f} and d_{nm} to h_{n}^{tf}, H_{n}^{f} and d_n, respectively, for $n = m$.

Interference Model: In intra-body environments, because of the non-negligible ultrasonic propagation delay that can be much larger than the time duration of a time slot, signals transmitted simultaneously by different transmitters do not reach the receiver at the same time in general. Hence, the interference experienced at each receiver depends not only on the channel model described above, but also on the concurrent interfering transmissions of other nodes. If the interfering nodes send their packets in a unsynchronized manner and each following a certain transmission probability profile that may vary from time to time (as will be discussed in detail in Section IV), the large propagation delay further creates time-varying interference statistics, which are difficult to capture.

To model the effect of non-aligned interference, we propose a new approach (that we refer to as *M-sampling method*) in which interference is characterized through a vector of measurements taken at multiple uniform-sampling time instants at each receiver during a given interval (i.e., time slot). Each receiver $n \in \mathcal{N}$ measures the received signal on each sub-channel $f \in \mathcal{F}$ in each time slot t at a set $\mathcal{M}_n^{tf}$ with $|\mathcal{M}_n^{tf}| = M$ of time instants. An illustration is shown in Fig. 2(a).

Because of the non-aligned nature of interference, a signal from session $n \in \mathcal{N}$ that arrives at its intended receiver at the l-th measurement instant in time slot t, with $l \in \mathcal{M}_n^{tf}$ for any $f \in \mathcal{F}$, can receive interference from the transmission of any session $m \in \mathcal{N}/n$ occurring during time slot $\tilde{t}(m,n,t,l)$, which might be different from t. Denote the transmission probability corresponding to $\tilde{t}(m,n,t,l)$ as $\alpha_m^{\tilde{t}(m,n,t,l)f}$ (also $\alpha_m^{\tilde{t}f}(n,t,l)$ for notational convenience). Let $I_n^{tf}(l), l \in \mathcal{M}_n^{tf}$, denote the aggregate interference measured by the receiver node of session $n \in \mathcal{N}$ on sub-channel $f \in \mathcal{F}$ at the l-th measurement point in time slot t. Then, $I_n^{tf}(l)$ can be expressed as

$$I_n^{tf}(l) = \sum_{m \in \mathcal{N}/n} P_m^0 h_{nm}^{tf} \hat{\alpha}_m^{\tilde{t}f}(n,t,l), \forall l \in \mathcal{M}_n^{tf}, \qquad (3)$$

where $\hat{\alpha}_m^{\tilde{t}f}(n,t,l) = 1$ with probability $\alpha_m^{\tilde{t}f}(n,t,l)$ and 0 with probability $1 - \alpha_m^{\tilde{t}f}(n,t,l)$.

Now we model the statistical characteristics of the interference level at each measurement time point l. With the previously discussed model of channel fading based on the generalized Nakagami distribution function, the probability

[3] A noticeable fitting gap can be observed between the model and the measurement results in the small-envelope region. To the best of our knowledge, there are no well-developed mathematical models that can be used to characterize accurately the statistics of ultrasonic intra-body channels. Our objective is to enable theoretical formulation and analysis of the stochastic channel access problem (will be presented in Sections IV and V) by presenting for the first time an ultrasonic intra-body channels model.

[4] A session m comprises a transmitter and a receiver, denoted as transmitter m and receiver m, respectively. In the following, we use transmitter (or receiver) m, the transmitter (or receiver) of session m and session m interchangeably while it will be clear based on the context if the transmitter or the receiver is referred to.

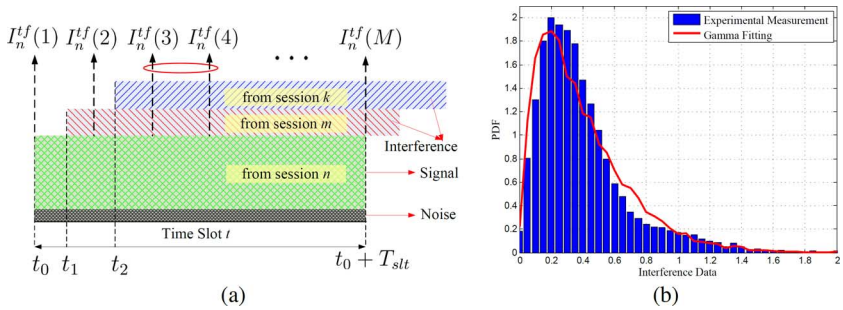

Fig. 2. (a) Interference model; (b) Validation of the Gamma-distribution-based interference model.

density function of the aggregate interference at each measurement instant $I_n^{tf}(l)$ can be characterized by a Gamma distribution function

$$\mathrm{P}[I_n^{tf}(l) = x] = \gamma_n^{tfl}(x) = x^{k_n^{tfl}} \frac{e^{-x/\theta_n^{tfl}}}{\Gamma(k_n^{tfl})(\theta_n^{tfl})^{k_n^{tfl}}}, \quad (4)$$

where $\Gamma(k_n^{tfl})$ is the gamma function as in (1), while k_n^{tfl} and θ_n^{tfl} are the shaping parameters of the Gamma distribution function depending on the transmission probabilities of all interferers $\hat{\alpha}_m^{\tilde{t}f}(n,t,l)$ in (3).

We validated the interference model through experiments, where we considered 10 interfering transmitters and one receiver randomly located around the kidney phantom. The power of each transmitter is set to 22 dBm, and the measurement period is set to 0.3 μs. We let each transmitter emit ultrasonic signals with probability 0.5 in each measurement period, and record the aggregate interference at the receiver. The probability density function of the measured interference is plotted in Fig. 2(b). Then, we fit the measured data using the Gamma distribution function with parameters k_n^{tfl} and θ_n^{tfl} in (4) estimated as

$$k_n^{tfl} = (\mu_n^{tf}(l))^2/(\sigma_n^{tf}(l))^2, \quad (5)$$

$$\theta_n^{tfl} = (\sigma_n^{tf}(l))^2/\mu_n^{tf}(l), \quad (6)$$

with $\mu_n^{tf}(l)$ and $\sigma_n^{tf}(l)$ being the mean and standard deviation of the recorded interference levels at the considered measurement time point l. Clearly, a Gamma distribution fits the experimental measurements very well.

Modeling the Temporal Correlation: Since each transmission lasts for a time slot duration T_{slt}, measurements of aggregate interference at different time instants in each time slot can be closely correlated with each other. Let $\eta_n^{tf}(l,\tilde{l})$ with $l,\tilde{l} \in \mathcal{M}_n^{tf}$ represent the correlation coefficient between $I_n^{tf}(l)$ and $I_n^{tf}(\tilde{l})$. Then, $\eta_n^{tf}(l,\tilde{l})$ can be expressed as

$$\eta_n^{tf}(l,\tilde{l}) = \frac{\mathrm{E}[(I_n^{tf}(l) - \mu_n^{tf}(l))(I_n^{tf}(\tilde{l}) - \mu_n^{tf}(\tilde{l}))]}{\sigma_n^{tf}(l)\sigma_n^{tf}(\tilde{l})}. \quad (7)$$

The interference measurements in $\mathcal{M}_n^{tf}$ can be grouped into $\{\tilde{\mathcal{M}}_n^{tf}(l)\}$ with each $\tilde{\mathcal{M}}_n^{tf}(l)$ consisting of a subset of measurements starting from the l-th. We adopt a threshold-based grouping policy, which groups a number of consecutive interference measurements $l, l+1, \ldots, \tilde{l}$ into $\tilde{\mathcal{M}}_n^{tf}(l)$ so that the correlation coefficient between the interference levels at any two measurements in the group (which are not necessarily adjacent to each other) is greater than a threshold denoted as η_n^{th}, i.e., $\eta_n^{tf}(l_1,l_2) \geq \eta_n^{\mathrm{th}}, l \leq l_1, l_2 \leq \tilde{l}$. An example of the measurement grouping is shown in Fig. 2(a), where $I_n^{tf}(3)$ and $I_n^{tf}(4)$ are grouped together since $\eta_n^{tf}(3,4) > \eta_n^{\mathrm{th}}$, and $I_n^{tf}(1)$ and $I_n^{tf}(2)$ are not grouped because $I_n^{tf}(2)$ suffers from interference from session m but not for $I_n^{tf}(1)$.

IV. Problem Formulation

Having developed the channel and interference models in the previous section, we now formulate and study a network-level optimization problem for ultrasonic intra-body communications.

Network Description: Consider an ultrasonic intra-body area network with a set $\mathcal{N}$ of concurrent sessions with $|\mathcal{N}| = N$, each consisting of a transmitter-receiver pair. The available spectrum is divided into a set $\mathcal{F}$ of orthogonal sub-channels with $|\mathcal{F}| = F$—the latter can be obtained on a code-division or frequency-division basis. Note that we consider multiple sub-channels to keep the system model as general as possible. The transmission time is divided into consecutive time slots, which are further grouped into consecutive frames each consisting of a set $\mathcal{T}$ of time slots with $|\mathcal{T}| = T$.

Let $\boldsymbol{R} = (R_n)_{n\in\mathcal{N}}$ represent the data generation profile, i.e., the transport-layer data allowed in the network. Then, each source node $n \in \mathcal{N}$ introduces data in its queue at an average rate of R_n [bit/s]. Because of the fast variability and high propagation delay of the ultrasonic channel, *we assume that each session can obtain only statistical channel state information (CSI) at the transmitter side (i.e., no fast feedback is available)*. Therefore, unlike in traditional RF communications, each transmitter adopts a stochastic policy (based only on the estimated statistics of interference at the receiver, and not on its instantaneous value), to decide whether to transmit in a specific time slot and over which sub-channel to transmit. Let $\boldsymbol{\alpha}_n^t = (\alpha_n^{tf})_{f\in\mathcal{F}}$ denote the data transmission vector of transmitter $n \in \mathcal{N}$ in time slot $t \in \mathcal{T}$, where α_n^{tf} represents the probability that session n transmits a packet over sub-channel $f \in \mathcal{F}$. Then, the transmission profile of session $n \in \mathcal{N}$ in a time frame denoted as $\boldsymbol{\alpha}_n$ can be written as $\boldsymbol{\alpha}_n = (\boldsymbol{\alpha}_n^t)_{t\in\mathcal{T}}$. Let $\boldsymbol{\alpha}$ represent the transmission profile of all sessions in $\mathcal{N}$ and $\boldsymbol{\alpha}_{-n}$ represent the transmission policy vector of all sessions except n. Then, $\boldsymbol{\alpha}$ and $\boldsymbol{\alpha}_{-n}$ can be written as $\boldsymbol{\alpha} = (\boldsymbol{\alpha}_n)_{n\in\mathcal{N}}$ and $\boldsymbol{\alpha}_{-n} = (\boldsymbol{\alpha}_m)_{m\in\mathcal{N}/n}$, respectively. Note that this model includes deterministic policies (i.e., in which the probability to transmit over a specific time slot or channel is equal to one) as a special case.

Let $U_n(R_n, \boldsymbol{\alpha}_n, \boldsymbol{\alpha}_{-n})$ represent the throughput of session $n \in \mathcal{N}$, which depends on its data generation rate R_n, transmission profile $\boldsymbol{\alpha}_n$ and also on the transmission profiles of all interfering sessions in $\mathcal{N}/n$. Then, the objective of each transmitter $n \in \mathcal{N}$ is to maximize its throughput $U_n(R_n, \boldsymbol{\alpha}_n, \boldsymbol{\alpha}_{-n})$

by jointly adjusting its data generation rate R_n and the transmission profile $\boldsymbol{\alpha}_n$, based on the statistical behavior of the observed interference caused by other interfering transmitters. To formalize the optimization problem, next we derive the mathematical expression for throughput $U_n(R_n, \boldsymbol{\alpha}_n, \boldsymbol{\alpha}_{-n})$.

Throughput Derivation: Due to the non-aligned interference as shown in Fig. 2(a), the experienced signal-to-interference-plus-noise ratio (SINR) in a time slot does not remain constant even if the channel is assumed to be slow-fading. This results in a fast-fading channel in each time slot.[5] If the measurement instants in each time slot are uniformly spaced,[6] then the outage probability of each session $n \in \mathcal{N}$ in time slot t over sub-channel $f \in \mathcal{F}$, denoted as $O_n^{tf}(\boldsymbol{\alpha}_{-n})$, can be expressed as [36]

$$O_n^{tf}(\boldsymbol{\alpha}_{-n}) \triangleq \mathrm{P}\left[\sum_{l \in \mathcal{L}(\mathcal{M}_n^{tf})} \frac{|\tilde{\mathcal{M}}_n^{tf}(l)|}{|\mathcal{M}_n^{tf}|} C(n,t,f,l) < R_n^0\right] \quad (8)$$

where $\mathcal{L}(\mathcal{M}_n^{tf})$ represents the set of beginning measurements of each group in $\{\tilde{\mathcal{M}}_n^{tf}\}$ defined in Section III, and

$$C(n,t,f,l) = B \log_2\left(1 + P_n^0 h_n^{tf} / [(\delta_n^f)^2 + I_n^{tf}(l)]\right) \quad (9)$$

represents the achievable capacity during measurement group $\tilde{\mathcal{M}}_n^{tf}(l)$, with $(\delta_n^f)^2$ being the ambient noise power at the receiver node of session $n \in \mathcal{N}$ over sub-channel $f \in \mathcal{N}$; B represents the bandwidth [Hz] of each sub-channel, and R_n^0 is the target rate required to transmit a packet in a time slot; $I_n^{tf}(l)$ is the aggregate interference given in (3). The distribution of $C(n,t,f,l)$ can be obtained with given distributions of channel fading coefficient h_n^{tf} and the aggregate interference $I_n^{tf}(l)$.

Then, the average capacity of session $n \in \mathcal{N}$, denoted as $C_n(\boldsymbol{\alpha}_n, \boldsymbol{\alpha}_{-n})$, can be expressed as

$$C_n(\boldsymbol{\alpha}_n, \boldsymbol{\alpha}_{-n}) = \frac{1}{|\mathcal{T}|} \sum_{t \in \mathcal{T}} C_n^t(\boldsymbol{\alpha}_n, \boldsymbol{\alpha}_{-n}), \quad (10)$$

with

$$C_n^t(\boldsymbol{\alpha}_n, \boldsymbol{\alpha}_{-n}) = \sum_{f \in \mathcal{F}} \alpha_n^{tf}(1 - O_n^{tf}(\boldsymbol{\alpha}_{-n})) R_n^0. \quad (11)$$

Finally, if we assume as in [37] that packet arrivals of each user $n \in \mathcal{N}$ follow a Poisson process with average arrival rate R_n [bit/s][7] and that the service time of each packet with length L_n bits follows an exponential distribution, the queue of each user $n \in \mathcal{N}$ can be modeled as a discrete-time $M/M/1$ queue [38, p. 162, §3.3]. Let $P_n^{\mathrm{dly}}(R_n, \boldsymbol{\alpha}_n, \boldsymbol{\alpha}_{-n})$ represent the packet loss rate of user n caused by exceeding the maximum queueing delay T_n^{th}. Then, $P_n^{\mathrm{dly}}(R_n, \boldsymbol{\alpha}_n, \boldsymbol{\alpha}_{-n})$ can be expressed as

$$P_n^{\mathrm{dly}}(R_n, \boldsymbol{\alpha}_n, \boldsymbol{\alpha}_{-n}) = e^{-(C_n(\boldsymbol{\alpha}_n, \boldsymbol{\alpha}_{-n}) - R_n)\frac{T_n^{\mathrm{th}}}{L_n}}, \quad (12)$$

and the throughput of each session $n \in \mathcal{N}$, denoted as $U_n(R_n, \boldsymbol{\alpha}_n, \boldsymbol{\alpha}_{-n})$, can be expressed as

$$U_n(R_n, \boldsymbol{\alpha}_n, \boldsymbol{\alpha}_{-n}) = R_n(1 - P_n^{\mathrm{dly}}(R_n, \boldsymbol{\alpha}) - P_n^{\mathrm{err}}), \quad (13)$$

where P_n^{err} represents the residual packet error rate due to non-perfect channel coding/decoding techniques, which is considered fixed in this work.

Problem Statement: So far, we have derived an expression for the throughput of each session. Then, the social objective is to maximize sum utility of all sessions $n \in \mathcal{N}$, with given energy budget $E_n^{\max}$ while keeping the radiated energy level within safety limits, by jointly controlling the stochastic channel access profile $\boldsymbol{\alpha}_n$ and regulating the data generation rate R_n, i.e.,

$$\text{Given}: E_n^{\max}, E_n^0, P_n^0, \forall n \in \mathcal{N} \quad (14a)$$

$$\underset{\boldsymbol{R}, \boldsymbol{\alpha}}{\text{Maximize}}: U(\boldsymbol{R}, \boldsymbol{\alpha}) = \sum_{n \in \mathcal{N}} U_n(R_n, \boldsymbol{\alpha}_n, \boldsymbol{\alpha}_{-n}) \quad (14b)$$

$$\text{Subject to}: \alpha_n^{tf} \geq 0, \forall n \in \mathcal{N}, \forall t \in \mathcal{T}, \forall f \in \mathcal{F} \quad (14c)$$

$$\alpha_n^{tf} \leq 1, \forall n \in \mathcal{N}, \forall t \in \mathcal{T}, \forall f \in \mathcal{F} \quad (14d)$$

$$\sum_{f \in \mathcal{F}} \alpha_n^{tf} \leq 1, \forall n \in \mathcal{N}, \forall t \in \mathcal{T} \quad (14e)$$

$$\sum_{t \in \mathcal{T}} \left(R_n E_n^0 + \sum_{f \in \mathcal{F}} \alpha_n^{tf} P_n^0\right) T_{\mathrm{slt}} \leq E_n^{\max}, \forall n \in \mathcal{N} \quad (14f)$$

where P_n^0 denotes the transmission power of user $n \in \mathcal{N}$,[8] T_{slt} represents the time slot duration, E_n^0 represents the energy [J] consumed by source node n to generate and process (e.g., A/D conversion, source encoding) one bit of data, and $E_n^{\max}$ denotes the maximum energy available in each time frame consisting of $|\mathcal{T}| = T$ consecutive time slots; constraint (14e) imposes that each session transmits on at most one sub-channel in each time slot on average, constraint (14f) imposes a balance between the energy needed for (i) data processing and generation and (ii) transmission for throughput maximization, under a given energy budget and limiting radiation to specific safety levels [4], [5].

Note that it is essential to incorporate rate control into the optimization framework, since in some scenarios of interest it might be very difficult to determine the optimal rate in advance. Consider for example a dynamic intra-body network with a set of miniaturized sensors cruising along the blood vessels to conduct multi-site measurement of physiological quantities of interest. As discussed in further detail in Section VII, without rate control, trivially allocating too high a portion of the energy budget to data generation leads to growing queueing delay that could result in high packet drop rates (therefore reducing the throughput).

[5]Different from fast fading in in-air radio-frequency communications, which is caused by the channel variation itself [36], here fast fading is caused by the non-aligned interference.

[6]Different measurement distributions will be studied in our future work, e.g., random distribution, compressive-sampling-based measurements.

[7]In this work, it is assumed that the data rate generation of different nodes are uncorrelated. For example, if nodes are performing different functions, say some are performing medical imaging while others are taking glucose level measurements, the resulting traffic is likely uncorrelated; conversely, if multiple nodes are involved in the same task, e.g., capturing images of the same tissue but from different angles, not only the data generation rates of different nodes would be correlated, but there would also be correlation in the data content. In the latter case, a more complicated traffic model needs to be developed to account for the correlations. This will be a topic of future research.

[8]We consider fixed transmission power since power control requires instantaneous CSI at the transmitter, which we assume to be unavailable.

V. Distributed Solution Algorithm

It is challenging to achieve the social objective formulated in (14a)–(14f) for many intra-body applications, as discussed in Section I, because of the lack of centralized control. In this section we design a lightweight, asynchronous and distributed resource allocation strategy, which we refer to as D-ROSA (Distributed Rate cOntrol and Stochastic channel Access), and discuss several issues related to the practical implementation and convergence of the algorithm. Then, to provide a performance benchmark for the proposed distributed algorithm, we derive the global optimum of the social problem based on a newly designed globally optimal but centralized solution algorithm, which will be briefly discussed in Section VI.

Algorithm: The D-ROSA algorithm is based on a local best-response strategy. Each transmitter iteratively solves the problem of joint rate control and transmission probability profile adaption based on a local observation of the second order statistics of the aggregate interference at the receiver.

We let $\Upsilon_n = \{(R_n, \boldsymbol{\alpha}_n)\}$ represent the domain set of session $n \in \mathcal{N}$, which consists of all possible combinations of R_n and $\boldsymbol{\alpha}_n$, as defined in (14c)–(14f). Then, for a given (fixed) transmission profile of all other sessions in $\mathcal{N}/n$, the individual optimization problem of session $n \in \mathcal{N}$ denoted as $\mathrm{OPT}(\Upsilon_n, U_n)$ with $U_n = U_n(R_n, \boldsymbol{\alpha}_n, \boldsymbol{\alpha}_{-n})$, can be represented as

$$\begin{array}{ll} \text{Given:} & E_n^{\max},\ E_n^0, P_n^0, \boldsymbol{\alpha}_{-n} \\ \underset{R_n, \boldsymbol{\alpha}_n}{\text{Maximize:}} & U_n(R_n, \boldsymbol{\alpha}_n, \boldsymbol{\alpha}_{-n}) \\ \text{Subject to:} & \text{Transmission constraints: (14c)} - \text{(14e)} \\ & \text{Energy constraint: (14f)} \end{array} \tag{15}$$

Then, the distributed best-response-based algorithm can be formalized as in Algorithm 1, where $\mathrm{SOL}(\Upsilon_n, U_n)$ represents the solution set of $\mathrm{OPT}(\Upsilon_n, U_n)$.

Algorithm 1 D-ROSA based on local best response

Data: $E_n^{\max}$, P_n^0, E_n^0, $\forall n \in \mathcal{N}$
(S.0): Choose any feasible $\boldsymbol{\alpha}_n^{(0)} \in \Upsilon_n$ and set $k = 0$
(S.1): If $\{\boldsymbol{\alpha}_n^{(k)}\}_{n\in\mathcal{N}}$ satisfies some stopping criterion, STOP.
(S.2): For each $n \in \mathcal{N}$, solve $\mathrm{OPT}(\Upsilon_n, U_n(\boldsymbol{\alpha}_n, \boldsymbol{\alpha}_{-n}^{(k)}))$.
(S.3): Let $\boldsymbol{\alpha}_n^{(k+1)} \in \mathrm{SOL}(\Upsilon_n, U_n(\boldsymbol{\alpha}_n, \boldsymbol{\alpha}_{-n}^{(k)}))$.
(S.4): Set $k \leftarrow k+1$ and goto (S.1).

In (S.1) of Algorithm 1, a stopping criterion can be the following: the change between the optimized transmission profile $\boldsymbol{\alpha}_n^{(k)}$ in two consecutive iterations is within a certain predefined error tolerance for all sessions in $\mathcal{N}$. As an alternative, we can set a limit on the maximum number of iterations. Note that Algorithm 1 is a Jacobi version of the distributed algorithm [19 p. 224, §3.4]. In practice, different sessions do not need to be synchronized when updating their own transmission probability profile, which results in a Gauss-Seidel-like implementation of the algorithm [19, p. 224, §3.4]. Note that at each iteration in Algorithm 1, each session solves an individual optimization problem formulated in (15), where the transmission probability profile of all other sessions $\boldsymbol{\alpha}_{-n}$ is assumed to be known as input, which is not the case in practice. Since we focus on fully distributed algorithms without any message exchange among different sessions, then a natural question that arises is: how can each session adjust its transmission probability profile based on the profile of the other sessions?

Proposition 1: It is sufficient for each session $n \in \mathcal{N}$ to estimate the statistical effects of aggregate interference from all other sessions in $\mathcal{N}/n$ with transmission profile $\boldsymbol{\alpha}_{-n}$ on its own throughput by recording the first- and second-order moments of the interference level observed at its intended receiver.

Proof: Recall that in Section III, we verified that the aggregate interference follows a Gamma distribution. Then, according to (5) and (6), the probability density function of interference can be exactly determined by (first-order) mean and (second-order) variance. □

Each session $n \in \mathcal{N}$ periodically transmits an updated estimate of the interference mean and variance back to its transmitter. Then, based on (3)–(11), the transmitter can calculate the outage probability profile $(O_n^{tf})_{t\in\mathcal{T}, f\in\mathcal{F}}$ and adjust its data generation rate R_n and transmission profile $\boldsymbol{\alpha}_n$ to maximize its own individual throughput $U_n(R_n, \boldsymbol{\alpha}_n, \boldsymbol{\alpha}_{-n})$ as given in (12) and (13). Since the expression in (13) is still non-concave, each optimization problem $\mathrm{OPT}(\Upsilon_n, U_n)$ is non-convex. In Theorem 1, we show however that the globally optimal solution of each $\mathrm{OPT}(\Upsilon_n, U_n)$ can still be obtained with polynomial-time algorithms.

Theorem 1: Each individual optimization problem in $\mathrm{OPT}(\Upsilon_n, U_n)$ can be solved by solving an equivalent convex optimization problem.

Proof: It can be proven that the objective function $U_n(R_n, \boldsymbol{\alpha}_n, \boldsymbol{\alpha}_{-n})$, with given $\boldsymbol{\alpha}_{-n}$, is a log-concave function. Moreover, all constraints in (14c)–(14f) are linear constraints, hence the resulting domain set is convex (also bounded and closed). Therefore, maximizing $U_n(R_n, \boldsymbol{\alpha}_n, \boldsymbol{\alpha}_{-n})$ is equivalent to maximizing its logarithm, which is a convex optimization problem, whose globally optimal solution can be solved in polynomial computational complexity using standard convex optimization techniques [39, §11]. Proof of the log-concavity of U_n follows the rule that affine mapping preserves convexity of function [39, P79, §3.2.2]. Please refer to Appendix A for more details. □

Convergence Analysis: We now provide some results on the convergence property of the proposed algorithm.

Theorem 2: Given the number of available channels $|\mathcal{F}|$ and the number of concurrent sessions $|\mathcal{N}|$, Algorithm 1 converges to a stationary point of the problem of joint rate control and stochastic channel access, if the number of time slots in each frame, i.e., $|\mathcal{T}|$, is sufficiently large. At this point, for each session there is no incentive to unilaterally deviate from its current transmission strategy.

Proof: The theorem can be proven by showing that the individual utility function $U_n(R_n, \boldsymbol{\alpha}_n, \boldsymbol{\alpha}_{-n})$ in (15) satisfies the condition in [40, Proposition 3]. Please refer to Appendix B for more details. □

Intuitively, with a large number of time slots in each frame, changing the transmission probability in a time slot for a session only affects the overall achievable capacity of the considered session slightly. Additionally, due to the linearity of (11) with respect to α_n^{tf}, each session assigns non-zero transmission

probability to only a subset of the jointly optimized time slots. The larger $|\mathcal{T}|$ is, the more likely it is that the time slot subsets for different sessions are disjoint with each other, which implies convergence of the algorithm. In practice, Algorithm 1 converges very fast to a stable zone with only limited $|\mathcal{T}|$, as shown in Section VII.

Practical Considerations: Note that Algorithm 1 *does not* require each receiver to send interference parameters (i.e., mean and variance) back to its transmitter at every time slot. Since the algorithm is designed based on a statistical characterization of the interference, feedback needs to be invoked only when there is a noticeable change in the statistical characteristics of interference compared with the last feedback, typically after tens or hundreds of time slots. Moreover, in each feedback message only mean and variance of the inference are transmitted. Furthermore, as discussed above, each transmitter only needs to solve a convex optimization problem with polynomial complexity with respect to the number of time slots in each frame upon receiving feedback. Therefore, the resulting communication and computational complexity is in practice low.

It is worth pointing out that since feedback information (including packet acknowledgement information) is short, it can be sent back to the transmitter based on reliable transmission schemes, e.g., using repetition coding [41], or CDMA with high spreading gain or other reliable coding techniques.

VI. Globally Optimal Algorithm

In Section V we have presented an algorithm to solve problem (15), which is a distributed version of the social joint rate control and channel access control problem formulated in (14a)–(14f). Then, a natural question is: how does the distributed solution compare to the global optimum of the social optimization problem? Next we answer this question by formulating the social optimization problem, proposing a centralized but globally optimal solution algorithm, and using the resulting global optimum as a benchmark for performance evaluation.

We develop a non-heuristic method for global optimization of the problem introduced above based on *a combination of the branch and bound framework and the reformulation linearization techniques (RLT)* [42, p. 297, §8]. The proposed algorithm searches for a globally optimal solution with predefined precision of optimality $0 < \varepsilon \leq 1$ which can be arbitrarily close to 1. If we denote the globally optimal objective function in (14b) as U^*, then the algorithm searches for an ε-optimal solution U that satisfies $U \geq \varepsilon U^*$.

The proposed algorithm searches for the optimal solution iteratively. At each iteration, the algorithm maintains a global upper bound $\mathrm{UP}_{\mathrm{glb}}$ and a global lower bound $\mathrm{LR}_{\mathrm{glb}}$ on the social objective U in (14b) such that

$$\mathrm{LR}_{\mathrm{glb}} \leq U^* \leq \mathrm{UP}_{\mathrm{glb}}. \tag{16}$$

Let $\Upsilon = \prod_{n\in\mathcal{N}} \Upsilon_n$ represent the Cartesian product of Υ_n defined in Section V with $n \in \mathcal{N}$, and define the initial search space as the overall domain set Υ. Then, the proposed algorithm maintains a set of sub-spaces $\widetilde{\Upsilon} = \{\Upsilon_i \subset \Upsilon, i = 1, 2, \ldots\}$, where i represents the iteration step of the algorithm. For any Υ_i, consider $\mathrm{UP}(\cdot)$ and $\mathrm{LR}(\cdot)$ as the upper and lower bounds on U in (14b) over sub-domain Υ_i. We refer to $\mathrm{UP}(\Upsilon_i)$ and $\mathrm{LR}(\Upsilon_i)$ as the local upper bound and local lower bound, respectively. Then, the global upper and lower bounds can be updated as

$$\mathrm{UP}_{\mathrm{glb}} = \max_i\{\mathrm{UP}(\Upsilon_i)\}, \tag{17}$$

$$\mathrm{LR}_{\mathrm{glb}} = \max_i\{\mathrm{LR}(\Upsilon_i)\}. \tag{18}$$

For example, at the beginning, i.e., $i = 0$, the set of sub-domains $\widetilde{\Upsilon}$ is initialized to $\{\Upsilon\}$, i.e., $\widetilde{\Upsilon} = \{\Upsilon\}$, and $\mathrm{UP}_{\mathrm{glb}}$ and $\mathrm{LR}_{\mathrm{glb}}$ are initialized to be $\mathrm{UP}(\Upsilon)$ and $\mathrm{LR}(\Upsilon)$, respectively. The algorithm partitions Υ into two sub-domains. For $\Upsilon_i,\ i = 1, 2$, the algorithm calculates $\mathrm{UP}(\Upsilon_i)$ and $\mathrm{LR}(\Upsilon_i)$, respectively. Then, the algorithm updates the global upper and lower bounds as follows

$$\mathrm{UP}_{\mathrm{glb}} = \max\{\mathrm{UP}(\Upsilon_i),\ i = 1, 2\}, \tag{19}$$

$$\mathrm{LR}_{\mathrm{glb}} = \max\{\mathrm{LR}(\Upsilon_i), i = 1, 2\}. \tag{20}$$

If $\mathrm{UP}(\Upsilon_i) < \mathrm{LR}_{\mathrm{glb}}$, this indicates that the globally optimal solution U^* is not located in Υ_i, and hence Υ_i is removed from $\{\Upsilon\}$.

We use $\mathrm{UP}_{\mathrm{glb}}$ to drive the branch and bound technique and use $\mathrm{LR}_{\mathrm{glb}}$ to check how close the obtained solution is to U^* and decide when to terminate the algorithm. If $\mathrm{LR}_{\mathrm{glb}} \geq \varepsilon \cdot \mathrm{UP}_{\mathrm{glb}}$, the algorithm terminates and sets the optimal objective U in (14b) to $U = \mathrm{LR}_{\mathrm{glb}}$. Otherwise, the algorithm chooses one sub-domain from $\widetilde{\Upsilon}$ and further partitions it into two sub-domains through *variable partition* (see Appendix C for more details), calculates $\mathrm{UP}(\cdot)$ and $\mathrm{LR}(\cdot)$, and updates the $\mathrm{UP}_{\mathrm{glb}}$ and $\mathrm{LR}_{\mathrm{glb}}$ as in (17) and (18). In our algorithm, we select the Υ_i with the highest local upper bound from $\widetilde{\Upsilon}$, i.e., $i = \arg\max_i \mathrm{UP}(\Upsilon_i)$. Based on the update criterion of $\mathrm{UP}_{\mathrm{glb}}$ and $\mathrm{LR}_{\mathrm{glb}}$ in (17) and (18), the gap between $\mathrm{UP}_{\mathrm{glb}}$ and $\mathrm{LR}_{\mathrm{glb}}$ converges to 0 as the domain-partition progresses. Furthermore, from (16), $\mathrm{UP}_{\mathrm{glb}}$ and $\mathrm{LR}_{\mathrm{glb}}$ converge to the globally maximal objective function U^*.

The branch-and-bound framework requires that, for given Υ_i, the $\mathrm{UP}(\Upsilon_i)$ and $\mathrm{LR}(\Upsilon_i)$ should be easy to calculate. To determine $\mathrm{UP}(\cdot)$, we rely on *convex relaxation*, i.e., we relax the original nonlinear non-convex problem into a convex problem that is easy to solve using the standard convex programming techniques. For $\mathrm{LR}(\cdot)$, through *local search* we obtain a feasible solution starting from the relaxed solution and set the corresponding sum-throughput as the local lower bound. Readers are referred to Appendix C for details of convex relaxation and local search.

VII. Performance Evaluation

In this section, we evaluate the performance of D-ROSA in terms of throughput, optimality and convergence. Some key simulation parameters are summarized in Table II for the reader's convenience. For performance comparison, we implemented Aloha and its variations. To the best of our knowledge, there are no other existing schemes designed for ultrasonic networking in intra-body environments. Moreover, we do not compare against CSMA/CA-based schemes because carrier sensing is known to be ineffective with high propagation delays [43]. Specifically, in addition to D-ROSA,

TABLE II
SIMULATION PARAMETERS

Para.	Physical Meaning	Value
	Communication area	$40 \times 40 \times 60$ (cm^3)
	Number of nodes	4, 8, 6, 10, 20, 50
β	Amplitude attenuation coefficient	0.1 (ultrasonic propagation in blood)
$F = \lvert\mathcal{F}\rvert$	Number of sub-channels	1, 2
$T = \lvert\mathcal{T}\rvert$	Number of time slots in a frame	1, 3, 4, 5, 7, 9, 11
R_n	Data generation rate	2, 4, 6, 8, 10, 30, 50, 80, 110 (kbit/s)
B	Sub-channel Bandwidth	50 (kHz)
L_n	Packet length	100 (bit)
T_{slt}	Time slot duration	0.5×10^{-3} (s)

we also implemented four competing schemes, three distributed and one centralized: (i) a variation of D-ROSA that does not consider rate control (ROSA-WoRC), i.e., a fixed data generation rate is considered that takes value from $\{0, 2, 4, 6, 8, 10, 30, 50, 70, 90, 110\}$ kbit/s; (ii) Aloha with optimized persistence probability for each session in each time slot (Aloha-Opt); the probability is set to the optimal transmission profile obtained by solving the social optimization problem in (14a)–(14f) but considering only a single time slot in each frame; (iii) Aloha-Opt without considering rate control (Aloha-WoRC); the data generation rate is the same as that in ROSA-WoRC; and (iv) the globally optimal solution algorithm (referred to as C-ROSA) designed in Section VI.

Case Study: First, as a case study we show the effect of multi-slot joint optimization on the individual throughput performance for a five-session intra-body network, as shown in Fig. 3. We observe that significant throughput gains can be obtained by D-ROSA compared with single-slot-based channel access (Aloha-Opt). For example, a 5× throughput gain is obtained by session 2. For session 2, a throughput of 19.59 kbit/s is achieved by transmitting with probability 1 and 0.23 in the second and third time slot in each frame, while keeping silent in the first and fourth (as indicated in the numerator in the figure). In the single-slot optimization, the session chooses to access the channel with probability 0.6318 in every time slot, and as a result, a throughput of only 3.86 kbit/s can be achieved. By averaging over the five sessions, a 3.3× throughput is achieved by D-ROSA. Indeed, we found that avoiding interference by adding a guard band to each time slot as proposed in [21] for underwater acoustic networks can be a natural outcome of optimizing the transmission strategy based on our framework. However, our framework leads to fully distributed solutions, while the approach in [21] needs global network information, and hence is not suited for fast time-varying networks.

Additional examples are presented in Figs. 4(a) and 4(b) by considering mobility of the transmitters. We consider three interfering sessions, and let each transmitter move randomly within a certain area (e.g., the targeted area of spatial-, temporal- and dosage-controlled medical applications [16]) following the Random waypoint model [44], as shown by the movement trajectory in Fig. 4(a). From Fig. 4(b) we can see that, D-ROSA considerably outperforms Aloha-Opt (i.e., Aloha with individually optimized persistence probability) in terms of individual

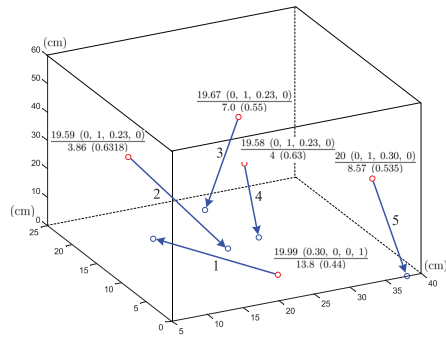

Fig. 3. Individual throughput and transmission probability profile with 5-sessions.

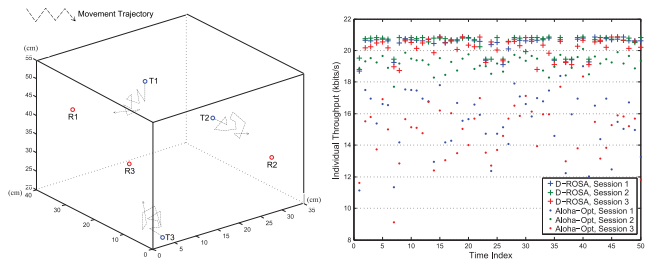

(a) (b)

Fig. 4. (a) The transmitter of each session moves following the Random waypoint model [44]; (b) Individual throughput by D-ROSA and Aloha-Opt in scenario (a).

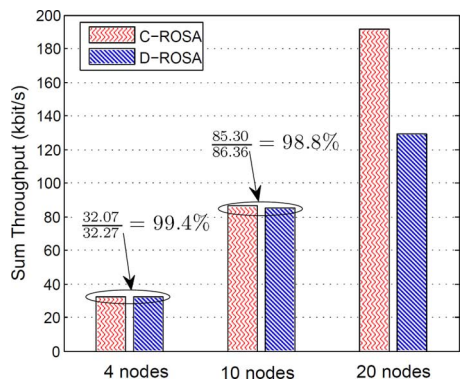

Fig. 5. Throughput comparison between D-ROSA and C-ROSA.

throughput in all tested network topologies and for all the three sessions.

Optimality and Convergence: Optimality and convergence properties of D-ROSA are studied in Figs. 5 and 6, respectively. From Fig. 5 we see that D-ROSA achieves nearly-optimal sum throughput in intra-body networks with a moderate number of nodes. For example, in 10-node intra-body networks 98.8% of the global optimum can be achieved by D-ROSA. Results also indicate a moderate performance gap between D-ROSA and C-ROSA when the number of nodes is large, e.g., around 70% of the optimum can be achieved. Note that this is achieved in a distributed way and with no message exchange. Cooperative strategies, requiring however message exchange among different sessions, were shown in our previous work to be able to partially fill this gap. However, for low densities of nodes that are envisioned in most practical applications, lightweight strategies with

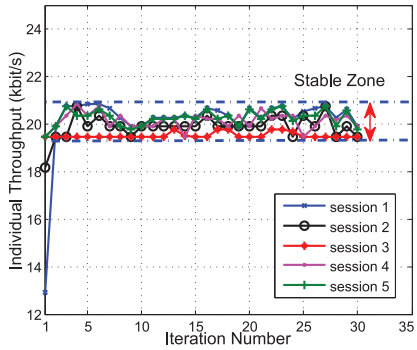

Fig. 6. The distributed algorithm converges to a stable zone very quickly.

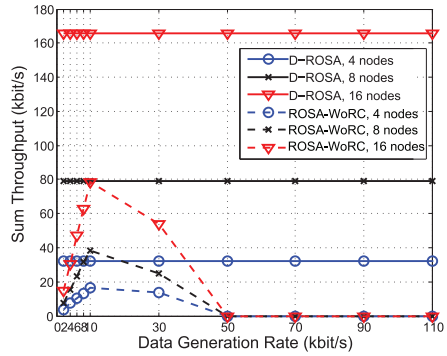

Fig. 8. Sum throughput against data generation rate with different number of nodes.

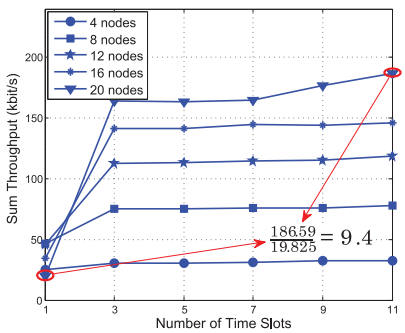

Fig. 7. Sum throughput achieved with different number of time slots in a frame and number of nodes.

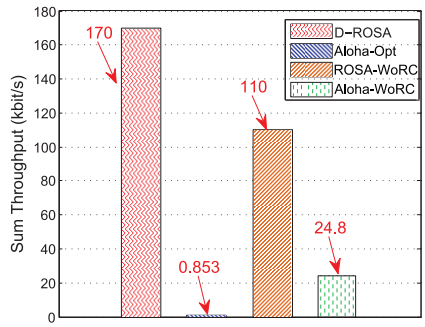

Fig. 9. Sum Throughput of different algorithms in a 50-node network.

minimal message exchange like D-ROSA seem to be more appealing. From Fig. 6, we see that D-ROSA can quickly converge to a stable zone (always within several iterations in the tested instances).

The effect of multi-slot optimization on sum throughput is further studied in Fig. 7, with T varying from 1 to 11 in steps of 2. By comparing the case $T = 3$ with $T = 1$, we observe that D-ROSA always obtains throughput gains. Also, in an intra-body network with a moderate number of nodes, e.g., $4 - 16$ in Fig. 7, jointly optimizing more than three time slots can only slightly increase the sum throughput. This is because in a network with little or moderate interference, a lower number of time slots is sufficient to provide the degrees of freedom needed by the involved sessions to avoid creating excessive interference to one another. An extreme case is the single-session network without interference, where there is no need for the session to perform multi-slot joint optimization. The benefit is more obvious in a high-interference network, e.g., in a 20-node intra-body network, where a maximum $9.4\times$ throughput gain can be achieved by jointly optimizing over 11 time slots.

The impact of rate control on the sum throughput is studied in Fig. 8, with 4, 8 and 16 nodes, and data generation rate R_n fixed to different values from 0 to 110 kbit/s (for the algorithm ROSA-WoRC). Compared with D-ROSA, the sum throughput of ROSA-WoRC degrades considerably once the data generation rate R_n is fixed to a given value for each session. While smaller values of R_n directly degrade the sum throughput, injecting too much data into the network leads to a more congested queue and also less energy available for data transmission with the total energy constraint in (14f). Note that, results in Fig. 8 are averaged over 100 simulations by varying the network topology. For a given specific intra-body network, if the rate R_n can be carefully tailored, e.g., fixed to the optimum, then the resulting throughput of ROSA-WoRC will coincide with D-ROSA. Doing so however is less flexible in practice for dynamic networks. For example, to measure in real-time specific blood components (e.g., the level of glucose) or to monitor certain tissues for micro-range and even multi-view imaging, a set of implanted sensors may need to move around as in Fig. 4(a), or cruise within a certain body area along blood vessels to conduct multi-point measurements. In this case, it would be very difficult to determine the optimal sampling rate in advance.

In Fig. 9, we compare the sum throughput achieved by the four distributed algorithms (D-ROSA, Aloha-Opt, ROSA-WoRC, and Aloha-WoRC) in a 50-node network. While, as expected, D-ROSA outperforms all the others, it is somewhat surprising that the throughput achieved by Aloha-Opt can be much lower than that of Aloha-WoRC. This implies that, in a high-interference network, rate control must be jointly applied with multi-slot optimization, or otherwise each session will inject large amounts of data into the network to optimize its own individual throughput, while the other sessions have no way to avoid the resulting high interference by Aloha-Opt based on which each session optimizes its transmission probability by considering single time slot only.

Testbed Results: Testbed experiments have also been conducted, with the objective of investigating if the throughput gain, compared to single-time-slot-based channel access, can be achieved by jointly optimizing the channel access over multiple time slots in D-ROSA and how the gain varies with the

number of time slots in each frame, by considering real ultrasonic intra-body channels (mimicked using a kidney phantom) and real state-of-the-art transmission schemes.

We first briefly introduce the experimental setup. The experiment consists of two ultrasonic nodes that communicate through a human-kidney phantom. Two ultrasonic transducers are located on opposite sides of the phantom at a distance of 10 cm. Time is divided in slots of 100 ms each, and each session can transmit at most one packet of 96 bytes per time slot. At the physical layer, we have implemented an orthogonal frequency-division multiplexing (OFDM) transmission scheme. We set the number of total subcarriers to 64, of which 48 are actually used for data transmission, over a bandwidth of approximately 200 kHz centered around 5 MHz, i.e., the central frequency of the ultrasonic transducer in use. The cyclic prefix is set to 16 samples. Each subcarrier is BPSK-modulated. This results in a physical layer data rate of approximately 120 kbit/s. At this stage, only stochastic channel access has been implemented on the test bed.

To guarantee repeatability of the experiments, we generate interference from co-located transceivers by artificially injecting interference at the transmitter, and multiplying each session for a stochastic component that follows a Nakagami distribution (please refer to Section III for validation of the channel model). We consider a maximum of five concurrent interfering sessions. In each time slot, each session transmits with a probability $p \in \{0.35, 0.5, 0.65, 0.8\}$. The number of time slots in each frame is varied from 1 to 9, and we set to 3 the number of packets available in each session queue that need to be transmitted within a time frame.

The experiment is divided in two stages. In the first stage, the transmitting node transmits in consecutive time slots while the receiver estimates the corresponding packet drop rate for each time slot. The estimate is sent to the transmitter, that decides accordingly the optimal transmission schedule. In the second stage, the transmitting node transmits the 3 packets in queue in each time frame according to the optimal transmission schedule obtained. At the receiver, we evaluate the performance of the resource allocation strategy in terms of packet drop rate (or packet delivery ratio).

In Fig. 10, we plot the packet drop rate against the number of time slots in each frame. We consider two scenarios with different interference levels, i.e., $SINR = 13$ dB in Fig. 10 (top) and $SINR = 10$ dB in Fig. 10 (bottom). For comparison, we compare D-ROSA with a random channel access, where the transmitting node selects randomly three time slots in a time frame to transmit. We observe that the resulting packet drop ratio consistently decreases as more time slots are jointly considered. When jointly considering 9 time slots, up to 10 times lower packet drop rate can be achieved compared to random channel access in the case of $SINR = 13$ dB, while 6 times lower than for $SINR = 10$ dB.

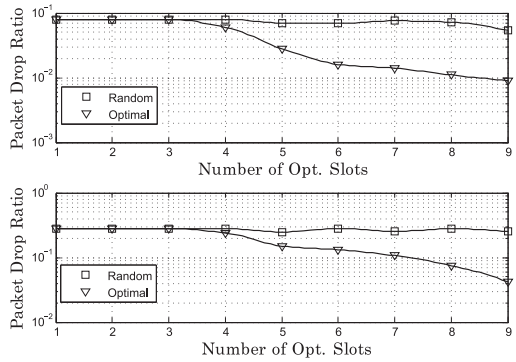

Fig. 10. Testbed validation: packet drop rate against the number of time slots in each frame with different levels of interference, $SINR = 13$ dB(top) and $SINR = 10$ dB (bottom).

VIII. Conclusions

We investigated for the first time algorithms for cross-layer control of functionalities in ultrasonic intra-body area networks. We focused on the design of lightweight, asynchronous, and distributed algorithms for joint stochastic channel access and rate control optimization, with the objective of maximizing the network throughput for a given energy budget. We first developed a statistical model of the spatial and temporal variability of ultrasonic interference. Then, we formulated a throughput maximization problem under energy budget constraints and proposed a distributed solution algorithm. Extensive simulation results showed considerable throughput gains compared with Aloha-based channel access, and that separate rate control could lead to rather poor performance in intra-body environments. Preliminary testbed results have also been presented to validate effectiveness of the algorithm.

It is worth pointing out that, the current testbed is equipped with only two transducers and a static Kidney phantom. To support more realistic validations, a new testbed needs to be developed with a phantom that can move as real human tissues and with a larger number of transducers. Another research subject in future is to develop mm-size miniaturized transducers to enable deployment of large-scale intra-body networks, e.g., with tens of and even more nodes as discussed in this paper. Other possible future research will be incorporating reliability (e.g., link layer retransmissions) and layer-3 routing into the network model and analysis.

Appendix

A. Proof of Log-Concavity

Define $\widetilde{U}_n \triangleq \log(U_n(R_n, \boldsymbol{\alpha}_n, \boldsymbol{\alpha}_{-n}))$, then we only need to show that $\widetilde{U}_n$ is a concave function with R_n and $\boldsymbol{\alpha}_n$, with given $\boldsymbol{\alpha}_{-n}$. To this end, we rewrite $\widetilde{U}_n$ as

$$\begin{aligned}\widetilde{U}_n &= \log\left(R_n(1 - P_n^{dly}(R_n, \boldsymbol{\alpha}_n, \boldsymbol{\alpha}_{-n}) - P_n^{err})\right) \\ &= \log\left(R_n\right) - (C_n(\boldsymbol{\alpha}_n, \boldsymbol{\alpha}_{-n}) - R_n)T_n^{th}/L_n \\ &\quad + \underbrace{\log\left((1 - P_n^{err})e^{(C_n(\boldsymbol{\alpha}_n, \boldsymbol{\alpha}_{-n}) - R_n)\frac{T_n^{th}}{L_n}} - 1\right)}_{A_n}. \quad (21)\end{aligned}$$

Since the first and second items in the right-hand side of (21) are linear, we only need to show that the third item denoted as A_n is concave.

Let $y_n(R_n, \boldsymbol{\alpha}) = C_n(\boldsymbol{\alpha}_n, \boldsymbol{\alpha}_{-n}) - R_n$, then it can be proven, by deriving the second-order derivative of A_n with respect to y_n, that A_n is a concave function of y_n. Moreover, from (10) and (11) we have that, with given $\boldsymbol{\alpha}_{-n}$, $y_n(R_n, \boldsymbol{\alpha}_n, \boldsymbol{\alpha}_{-n})$ is an

affine function of R_n and $\boldsymbol{\alpha}_n$. Then, based on the fact that composition with an affine mapping preserves convexity of function [39, §3.2.2], we have A_n is a concave function of R_n and $\boldsymbol{\alpha}_n$.

B. Proof of Theorem 2

We first construct a $|\mathcal{N}| \times |\mathcal{N}|$ real matrix $\Phi_{\widetilde{U}}$ as follows

$$[\Phi_{\widetilde{U}}]_{nm} \triangleq \begin{cases} -\mu_n^{\max}, & \text{if } n = m, \\ -\nu_{nm}^{\max}, & \text{otherwise}, \end{cases} \tag{22}$$

where $\mu_n^{\max} \triangleq \sup_{(\mathbf{R},\boldsymbol{\alpha})\in\Upsilon} \lambda_{\text{most}}(\mathrm{H}_{nn})$ and $\nu_{nm}^{\max} \triangleq \sup_{(\mathbf{R},\boldsymbol{\alpha})\in\Upsilon} \|\mathrm{H}_{nm}\|$, with H_{nn} being the Hessian matrix of $\widetilde{U}_n$, H_{nm} the Jacobi matrix with respect to $(R_n, \boldsymbol{\alpha}_n)$ of the gradient function of $\widetilde{U}_m$, $\lambda_{\text{most}}(\mathrm{H}_{nn})$ the greatest eigenvalue of H_{nn}, and $\Upsilon = \prod_{n\in\mathcal{N}} \Upsilon_n$ being the Cartesian product of all individual domain sets Γ_n. Then, to prove the theorem, we only need to show that $[\Phi_{\widetilde{U}}]_{nm}$ in (22) is a P-matrix, and further it is sufficient to show the following condition holds true [40, P7, Proposition 3]

$$-\mu_n^{\max} > \sum_{m\in\mathcal{N}/n} \nu_{nm}^{\max}. \tag{23}$$

From (21), (10) and (11), each element of H_{nn}, i.e., the second derivative of $\widetilde{U}_n$ with respect to R_n and α_n, can be written as

$$\frac{\partial^2 \widetilde{U}_n}{\partial (R_n)^2} = -\frac{1}{(R_n)^2} + \frac{\partial^2 A_n}{\partial y_n^2} \tag{24}$$

$$\frac{\partial^2 \widetilde{U}_n}{\partial R_n \partial \alpha_n^{tf}} = -\frac{\partial^2 A_n}{\partial y_n^2}\left[\frac{R_n^0}{|\mathcal{T}|}(1 - O_n^{tf}(\boldsymbol{\alpha}_{-n}))\right] \tag{25}$$

$$\frac{\partial^2 \widetilde{U}_n}{\partial (\alpha_n^{tf})^2} = \frac{\partial^2 A_n}{\partial y_n^2}\left[\frac{R_n^0}{|\mathcal{T}|}(1 - O_n^{tf}(\boldsymbol{\alpha}_{-n}))\right]^2 \tag{26}$$

with A_n and y_n defined in Appendix A, $|\mathcal{T}|$ and R_n^0 being parameters in (10) and (11), and $O_n^{tf}(\boldsymbol{\alpha}_{-n})$ defined in (8). Each element of Jacobi matrix H_{nm} can be written as

$$\frac{\partial^2 \widetilde{U}_m}{\partial R_m \partial R_n} = \frac{\partial^2 \widetilde{U}_m}{\partial \alpha_m^{tf} \partial R_n} = 0 \tag{27}$$

$$\frac{\partial^2 \widetilde{U}_m}{\partial R_m \partial \alpha_n^{tf}} = -\frac{\partial^2 A}{\partial (y_m)^2}\frac{\alpha_m^{tf} R_m^0}{|\mathcal{T}|}\frac{\partial O_m^{tf}}{\partial \alpha_n^{tf}} \tag{28}$$

$$\frac{\partial^2 \widetilde{U}_m}{\partial \alpha_m^{tf} \partial \alpha_n^{tf}} = \left[\frac{R_m^0}{|\mathcal{T}|}(1 - O_m^{tf}(\boldsymbol{\alpha}_{-m}))\right]\frac{\partial^2 A}{\partial (y_m)^2}\frac{\alpha_m^{tf} R_m^0}{|\mathcal{T}|}\frac{\partial O_m^{tf}}{\partial \alpha_n^{tf}} - \left(\frac{\partial A}{\partial y_m} - \frac{T_m^{th}}{L_m}\right)\frac{R_m^0}{|\mathcal{T}|}\frac{\partial O_m^{tf}}{\partial \alpha_n^{tf}}. \tag{29}$$

We can see from (24)–(29) that, as the number of time slots in each frame $|\mathcal{T}|$ increases, the determinate the Hessian matrix H_{nn} turns to be dominated by only $\frac{\partial^2 \widetilde{U}_n}{\partial (R_n)^2}$ in (24), and the Jacobi matrix H_{nm} turns to be a zero matrix. In the case of sufficiently large $|\mathcal{T}|$, we have

$$\mu_n^{\max} \approx -\frac{1}{(R_n)^2} + \frac{\partial^2 A_n}{\partial y_n^2}, \forall n \in \mathcal{N} \tag{30}$$

$$\nu_{nm}^{\max} \approx 0, \forall n, m \in \mathcal{N} \tag{31}$$

and hence condition (23) holds true since $\frac{\partial^2 A_n}{\partial y_n^2} \leq 0$ for the concave function $\widetilde{U}_n$.

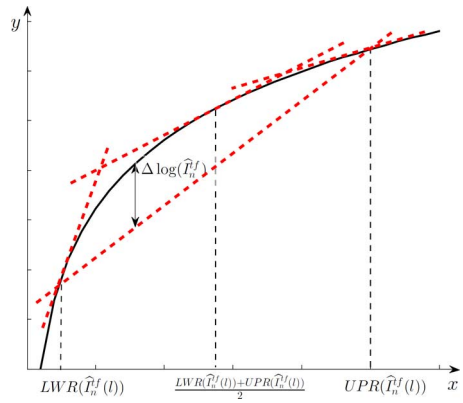

Fig. 11. Approximation the logarithm function using four lines: the secant connecting the points corresponding to $x = LWR(\widehat{I}_n^{tf})$ and $x = UPR(\widehat{I}_n^{tf})$, three tangents corresponding to $x = LWR(\widehat{I}_n^{tf})$, $UPR(\widehat{I}_n^{tf})$ and $\frac{LWR(\widehat{I}_n^{tf})+UPR(\widehat{I}_n^{tf})}{2}$.

C. Centralized Solution Algorithm

We describe the three key components of the centralized solution algorithm, i.e., convex relaxation, variable partition, and local search.

1) Convex Relaxation: To relax the social optimization problem in (14a)–(14f) to be convex, we need to relax all non-convex items, including the non-concave capacity expression in (9), and the non-concave objective function in (13).

To relax the non-concave expression $C(n,t,f,l)$ in (9), we first rewrite it as

$$C(n,t,f,l) = \log_2\left((\delta_n^f)^2 + I_n^{tf}(l) + P_n^0 h_n^{tf}\right) - \log_2\left((\delta_n^f)^2 + I_n^{tf}(l)\right). \tag{32}$$

Since the first line of (32) is concave, it is sufficient to only relax the item in the second line. We chose to relax the logarithm with a set of linear constraints. Fig. 11 shows an illustration of the relaxation, where we use four lines, one secant and three tangent lines, to approximate the original logarithm function. The lower and upper bound of $\widehat{I}_n^{tf}(l) \triangleq (\delta_n^f)^2 + I_n^{tf}(l)$ can be easily calculated with given range of α_m^{tf} for each interfering session $m \in \mathcal{M}/n$ in a specific sub-domain. The relaxation error $\Delta\log(\widehat{I}_n^{tf}(l))$, defined as the gap between the relaxed value and the real value of the logarithm function, tends to zero as the sub-domain partition goes.

To relax the non-concave objective function in (13), we first introduce a new variable

$$\widehat{P}_n^{\text{dly}} \triangleq -P_n^{\text{dly}}(R_n, \boldsymbol{\alpha}_n, \boldsymbol{\alpha}_{-n}). \tag{33}$$

Then, the individual objective function in (13) can be rewritten as $U_n(R_n, \boldsymbol{\alpha}) = R_n(1 - P_n^{\text{err}}) + R_n\widehat{P}_n^{\text{dly}}$, where the first item in the right-hand side is linear while the second item can be relaxed using the RLT [42]. To this end, let $UPR(\widehat{P}_n^{\text{dly}})$, $UPR(R_n)$ and $LWR(\widehat{P}_n^{\text{dly}})$, $LWR(R_n)$ represent the upper and lower bounds of $\widehat{P}_n^{\text{dly}}$ and R_n, respectively, with given sub-domain Υ_i. Further, we introduce a new variable $\psi_n = R_n\widehat{P}_n^{\text{dly}}$, then the non-convex item $R_n\widehat{P}_n^{\text{dly}}$ can be relaxed by substituting ψ_n into the following four linear constraints,

$$(UPR(\widehat{P}_n^{\text{dly}}) - \widehat{P}_n^{\text{dly}})(UPR(R_n) - R_n) \geq 0, \tag{34}$$

$$(UPR(\widehat{P}_n^{\rm dly}) - \widehat{P}_n^{\rm dly})(R_n - LWR(R_n)) \geq 0, \quad (35)$$
$$(\widehat{P}_n^{\rm dly} - LWR(\widehat{P}_n^{\rm dly}))(UPR(R_n) - R_n) \geq 0, \quad (36)$$
$$(\widehat{P}_n^{\rm dly} - LWR(\widehat{P}_n^{\rm dly}))(R_n - LWR(R_n)) \geq 0. \quad (37)$$

Since $P_n^{\rm dly}(R_n, \boldsymbol{\alpha}_n, \boldsymbol{\alpha}_{-n})$ defined in (12) is a monotonic function with $R_n - C_n(\boldsymbol{\alpha}_n, \boldsymbol{\alpha}_{-n})$, the above upper and lower bounds $UPR(\widehat{P}_n^{\rm dly})$ and $LWR(\widehat{P}_n^{\rm dly})$ can be easily calculated by solving linear optimization problems.

Finally, we relax the equality constraint in (33) as

$$\widehat{P}_n^{\rm dly} \leq -P_n^{\rm dly}(R_n, \boldsymbol{\alpha}_n, \boldsymbol{\alpha}_{-n}), \quad (38)$$
$$\widehat{P}_n^{\rm dly} \geq LWR(\widehat{P}_n^{\rm dly}), \quad (39)$$

which result in a convex domain set since $-P_n^{\rm dly}$ in (38) is a concave function with respect to R_n and $C_n(\boldsymbol{\alpha}_n, \boldsymbol{\alpha}_{-n})$ in (10).

2) Variable Partition: We select the subproblem that has the highest local upper bound to partition. In this paper, we select the subproblem that has the highest local upper bound. The selected subproblem can be partitioned into two new subproblems by partitioning one of its variables, i.e., $\{\alpha_n^{tf}, n \in \mathcal{N}, t \in \mathcal{T}, f \in \mathcal{F}\}$. We select the variable that has the largest range and partition it in the middle, that is to select $(\alpha_n^{tf})^*$ such that

$$(\alpha_n^{tf})^* = \max_{n\in\mathcal{N}, t\in\mathcal{T}, f\in\mathcal{F}} (UPR(\alpha_n^{tf}) - LWR(\alpha_n^{tf})), \quad (40)$$

and partition it as

$$(\alpha_n^{tf})^{\rm M} = \frac{UPR((\alpha_n^{tf})^*) + LWR((\alpha_n^{tf})^*)}{2}, \quad (41)$$

which results in two new subproblems with domains of $[LWR((\alpha_n^{tf})^*) \quad (\alpha_n^{tf})^{\rm M}]$ and $[(\alpha_n^{tf})^{\rm M} \quad UPR((\alpha_n^{tf})^*)]$, respectively.

3) Local Search: We call the solution obtained through solving the relaxed optimization problem *relaxed solution*. Since the transmission profile $\boldsymbol{\alpha}$ corresponding to the relaxed solution is also feasible, we can obtain a lower-bound capacity based on (10), and then calculate the optimal R_n with given C_n for each $n \in \mathcal{N}$ by solving a convex optimization problem similar as in Algorithm 1.

REFERENCES

[1] Z. Guan, G. E. Santagati, and T. Melodia, "Ultrasonic intra-body networking: Interference modeling, stochastic channel access and rate control," in *Proc. IEEE Conf. Comput. Commun.*, Hong Kong, Apr. 2015, pp. 2425–2433.

[2] B. Latré, B. Braem, I. Moerman, C. Blondia, and P. Demeester, "A survey on wireless body area networks," *Wireless Netw.*, vol. 17, no. 1, pp. 1–18, Jan. 2011.

[3] T. Gao, D. Greenspan, M. Welsh, R. R. Juang, and A. Alm, "Vital signs monitoring and patient tracking over a wireless network," in *Proc. IEEE Int. Conf. Eng. Med. Biol. Soc.*, Shanghai, China, Sep. 2005, pp. 102–105.

[4] G. E. Santagati, T. Melodia, L. Galluccio, and S. Palazzo, "Ultrasonic networking for e-health applications," *IEEE Wireless Commun. Mag.*, vol. 20, no. 4, pp. 74–81, Aug. 2013.

[5] T. Hogg and R. A. Freitas, "Acoustic communication for medical nanorobots," *Nano Commun. Netw.*, vol. 3, no. 2, pp. 83–102, Feb. 2012.

[6] Medtronic, "Medtronic pain neurostimulation system," [Online]. Available: http://www.medtronic.com/

[7] St. Jude Medical, "The CardioMEMS HF system," [Online]. Available: http://www.sjm.com/cardiomems/

[8] Microsemi, "Implantable medical transceivers," [Online]. Available: http://www.microsemi.com/

[9] G. E. Santagati, T. Melodia, L. Galluccio, and S. Palazzo, "Medium access control and rate adaptation for ultrasonic intra-body sensor networks," *IEEE/ACM Trans. Netw.*, vol. 23, no. 4, pp. 1121–1134, Aug. 2015.

[10] G. E. Santagati and T. Melodia, "Sonar inside your body: Prototyping ultrasonic intra-body sensor networks," in *Proc. IEEE Conf. Comput. Commun.*, Toronto, ON, Canada, Apr. 2014, pp. 2679–2687.

[11] G. Oberholzer, P. Sommer, and R. Wattenhofer, "Spiderbat: Augmenting wireless sensor networks with distance and angle information," in *Proc. IEEE/ACM Int. Conf. Inf. Process. Sensor Netw.*, Chicago, IL, USA, Apr. 2011, pp. 211–222.

[12] F. L. Thurstone and H. E. Melton, "Biomedical ultrasonics," *IEEE Trans. Ind. Electron. Control Instrum.*, vol. IECI-17, no. 2, pp. 167–172, Apr. 1970.

[13] J. Hoyd-GiggNg *et al.*, "Progress towards the development of novel fabrication and assembly methods for the next generation of ultrasonic transducers," in *Proc. IEEE Electron. Syst.-Integration Technol. Conf., Maritim Pro Arte*, Berlin, Sep. 2010, pp. 1–6.

[14] A. Lanata, E. Scilingo, and D. D. Rossi, "A multimodal transducer for cardiopulmonary activity monitoring in emergency," *IEEE Trans. Inf. Technol. Biomed.*, vol. 14, no. 3, pp. 817–825, May 2010.

[15] R. Smith *et al.*, "Design and fabrication of ultrasonic transducers with nanoscale dimensions," *J. Phys.*, vol. 278, no. 1, pp. 1–4, Jan. 2011.

[16] S. Mura, J. Nicolas, and P. Couvreur, "Stimuli-responsive nanocarriers for drug delivery," *Nature Mater.*, vol. 12, pp. 991–1003, Nov. 2013.

[17] A. Y. Cheung and A. Neyzari, "Deep local hyperthermia for cancer therapy: External electromagnetic and ultrasound techniques," *Cancer Res. (Suppl.)*, vol. 44, no. 9, pp. 4736–4744, Oct. 1984.

[18] A. Kiourti, K. A. Psathas, and K. S. Nikita, "Implantable and ingestible medical devices with wireless telemetry functionalities: A review of current status and challenges," *Bioelectromagnetics*, vol. 35, no. 1, pp. 1–15, Jan. 2014.

[19] D. P. Bertsekas and J. N. Tsitsiklis, *Parallel and Distributed Computation: Numerical Methods*. Upper Saddle River, NJ, USA: Prentice-Hall, 1989.

[20] L. Galluccio, T. Melodia, S. Palazzo, and G. E. Santagati, "Challenges and implications of using ultrasonic communications in intra-body area networks," in *Proc. IEEE Int. Conf. Wireless On-Demand Netw. Syst.*, Courmayeur, Italy, Jan. 2012, pp. 182–189.

[21] A. Syed, W. Ye, J. Heidemann, and B. Krishnamachari, "Understanding spatio-temporal uncertainty in medium access with ALOHA protocols," in *Proc. ACM Int. Workshop Underwater Netw.*, Montreal, QC, Canada, Sep. 2007, pp. 41–48.

[22] X. Guo, M. Frater, and M. Ryan, "Design of a propagation-delay-tolerant MAC protocol for underwater acoustic sensor networks," *IEEE J. Ocean. Eng.*, vol. 34, no. 2, pp. 170–180, Apr. 2009.

[23] Z. Zhou, Z. Peng, J.-H. Cui, and Z. Jiang, "Handling triple hidden terminal problems for multichannel MAC in long-delay underwater sensor networks," *IEEE Trans. Mobile Comput.*, vol. 11, no. 1, pp. 139–154, Jan. 2012.

[24] M. Chitre, M. Motani, and S. Shahabudeen, "A scheduling algorithm for wireless networks with large propagation delays," in *Proc. IEEE Oceans*, Sydney, Australia, May 2010, pp. 1–5.

[25] B. Peleato and M. Stojanovic, "Distance aware collision avoidance protocol for ad-hoc underwater acoustic sensor networks," *IEEE Commun. Lett.*, vol. 11, no. 12, pp. 1025–1027, Dec. 2007.

[26] M. Chiang, S. Low, A. Calderbank, and J. Doyle, "Layering as optimization decomposition: A mathematical theory of network architectures," *Proc. IEEE*, vol. 95, no. 1, pp. 255–312, Jan. 2007.

[27] X. Lin and S. Rasool, "A distributed joint channel-assignment, scheduling and routing algorithm for multi-channel ad hoc wireless networks," in *Proc. IEEE Int. Conf. Comput. Commun.*, Anchorage, AK, USA, May 2007, pp. 1118–1126.

[28] Y. T. Hou, Y. Shi, and H. D. Sherali, "Optimal spectrum sharing for multi-hop software defined radio networks," in *Proc. IEEE Int. Conf. Comput. Commun.*, Anchorage, AK, USA, May 2007, pp. 1–9.

[29] X. Fang, D. Yang, and G. Xue, "Resource allocation in load-constrained multihop wireless networks," in *Proc. IEEE Int. Conf. Comput. Commun.*, Orlando, FL, USA, Mar. 2012, pp. 280–288.

[30] P.-K. Huang and X. Lin, "Improving the delay performance of CSMA algorithms: A virtual multi-channel approach," in *Proc. IEEE Int. Conf. Comput. Commun.*, Turin, Italy, Apr. 2013, pp. 2598–2606.

[31] J. Kwak, C.-H. Lee, and D. Y. Eun, "A high-order Markov chain based scheduling algorithm for low delay in CSMA networks," in *Proc. IEEE Int. Conf. Comput. Commun.*, Toronto, ON, Canada, Apr. 2014, pp. 1662–1670.

[32] Ettus Research, "USRP: Universal software radio peripheral," [Online]. Available: http://www.ettus.com/
[33] The Ultran Group, "Standard immersion ultrasonic transducers," [Online]. Available: http://www.ultrangroup.com/index.php/products/transducers/standard/
[34] CIRS, "CIRS: Kidney training phantom," [Online]. Available: http://www.cirsinc.com/products/all/81/kidney-training-phantom/
[35] A. Tipirneni, R. Song, R. B. Loeffler, and C. M. Hillenbrand, "Evaluation of the relationship between respiratory hepatic and renal motion using real-time MRI," *Proc. Int. Soc. Magn. Resonance Med.*, vol. 17, p. 2071, 2015.
[36] D. Tse and P. Viswanat, *Fundamentals of Wireless Communication*. New York, NY, USA: Cambridge Univ. Press, 2005.
[37] X. Zhu, E. Setton, and B. Girod, "Congestion-distortion optimized video transmission over ad hoc networks," *EURASIP Signal Process., Image Commun.*, vol. 20, no. 8, pp. 773–783, Sep. 2005.
[38] D. Bertsekas and R. Gallager, *Data Networks*. Upper Saddle River, NJ, USA: Prentice-Hall, 2000.
[39] S. Boyd and L. Vandenberghe, *Convex Optimization*. Cambridge, U.K.: Cambridge Univ. Press, 2004.
[40] G. Scutari, D. P. Palomar, F. Facchinei, and J.-S. Pang, "Monotone games for cognitive radio systems," in *Distributed Decision-Making and Control*, ser. Lecture Notes in Control and Information Sciences, A. Rantzer and R. Johansson, Eds. New York, NY, USA: Springer-Verlag, 2011.
[41] A. A. Ali and I. A. Al-Kadi, "On the use of repetition coding with binary digital modulations on mobile channels," *IEEE Trans. Veh. Technol.*, vol. 38, no. 1, pp. 14–18, Feb. 1989.
[42] H. D. Sherali and W. P. Adams, *A Reformulation-Linearization Technique for Solving Discrete and Continuous Nonconvex Problems*. Boston, MA, USA: Kluwer, 1999.
[43] D. Pompili, T. Melodia, and I. F. Akyildiz, "A CDMA-based medium access control for underwater acoustic sensor networks," *IEEE Trans. Wireless Commun.*, vol. 8, no. 4, pp. 1899–1909, Apr. 2009.
[44] T. Camp, J. Boleng, and V. Davies, "A survey of mobility models for ad hoc network research," *Wireless Commun. Mobile Comput.*, vol. 2, no. 5, pp. 483–502, Aug. 2002.

Zhangyu Guan (M'11) received the Ph.D. degree in communication and information systems from Shandong University, Jinan, China, in 2010.

He is currently a Postdoctoral Research Associate with the Department of Electrical and Computer Engineering, Northeastern University, Boston, MA, USA. He was a visiting Ph.D. student with the Department of Electrical Engineering, The State University of New York (SUNY) at Buffalo, Buffalo, NY, USA, from 2009 to 2010; he was a Lecturer with Shandong University from 2011 to 2014; and he was a Postdoctoral Research Associate with the Department of Electrical Engineering, SUNY Buffalo from November 2012 to August 2015. His current research interests are in cognitive radio and software-defined networking, wireless multimedia sensor networks, and underwater networks.

Dr. Guan has served as a TPC member for IEEE INFOCOM 2016, IEEE GLOBECOM 2015, IEEE ICNC 2012–2015, and IEEE VTC 2011-Fall and 2015-Fall, among others, and served as a reviewer for the IEEE TRANSACTIONS ON COMMUNICATIONS, the IEEE JOURNAL ON SELECTED AREAS IN COMMUNICATIONS, and the IEEE COMMUNICATIONS SURVEYS AND TUTORIALS, among others.

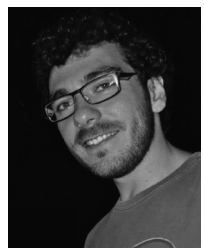

G. Enrico Santagati is a Ph.D. student with the Department of Electrical and Computer Engineering, Northeastern University, Boston, MA, USA. He is currently working with the Wireless Networks and Embedded Systems Laboratory under the guidance of Prof. Tommaso Melodia. He received the B.S. and M.S. degrees in telecommunication engineering from the University of Catania, Catania, Italy, in 2010 and 2012, respectively. His current research interests are in ultrasonic intra-body networks and software defined radios.

Tommaso Melodia (M'07) received the Ph.D. degree in electrical and computer engineering from the Georgia Institute of Technology, Atlanta, GA, USA, in 2007.

He is an Associate Professor with the Department of Electrical and Computer Engineering, Northeastern University, Boston, MA, USA. His research has been supported by the National Science Foundation, Air Force Research Laboratory, and the Office of Naval Research, among others. His current research interests are in modeling, optimization, and experimental evaluation of networked communication systems, with applications to ultrasonic intra-body networks, cognitive and cooperative networks, multimedia sensor networks, and underwater networks.

Prof. Melodia was a recipient of the National Science Foundation CAREER Award and coauthored a paper that was recognized as the ISI Fast Breaking Paper in the field of Computer Science for February 2009 and of Best Paper Awards of ACM WUWNet 2013 and 2015. He was the Technical Program Committee Vice Chair for IEEE GLOBECOM 2013 and the Technical Program Committee Vice Chair for Information Systems for IEEE INFOCOM 2013. He serves on the editorial boards of the IEEE TRANSACTIONS ON MOBILE COMPUTING, the IEEE TRANSACTIONS ON WIRELESS COMMUNICATIONS, the IEEE TRANSACTIONS ON MULTIMEDIA, and *Computer Networks*.